ResearchGate

See discussions, stats, and author profiles for this publication at: https://www.researchgate.net/publication/280112307

On design of multi-cell tubes under axial and oblique impact loads

Article *in* Thin-Walled Structures · October 2015

DOI: 10.1016/j.tws.2015.07.002

CITATIONS
239

READS
632

5 authors, including:

Jianguang Fang
University of Technology Sydney
127 PUBLICATIONS **6,111** CITATIONS

SEE PROFILE

Yunkai Gao
Tongji University
58 PUBLICATIONS **2,018** CITATIONS

SEE PROFILE

Guangyong Sun
Hunan University
257 PUBLICATIONS **16,509** CITATIONS

SEE PROFILE

Na Qiu
Tongji University
25 PUBLICATIONS **1,477** CITATIONS

SEE PROFILE

All content following this page was uploaded by Guangyong Sun on 10 May 2021.

The user has requested enhancement of the downloaded file.

Thin-Walled Structures 95 (2015) 115–126

Contents lists available at ScienceDirect

Thin-Walled Structures

journal homepage: www.elsevier.com/locate/tws

On design of multi-cell tubes under axial and oblique impact loads

Jianguang Fang [a,c], Yunkai Gao [a,*], Guangyong Sun [b,c,**], Na Qiu [a], Qing Li [c]

[a] School of Automotive Studies, Tongji University, Shanghai 201804, China
[b] State Key Laboratory of Advanced Design and Manufacture for Vehicle Body, Hunan University, Changsha 410082, China
[c] School of Aerospace, Mechanical and Mechatronic Engineering, The University of Sydney, Sydney, NSW 2006, Australia

ARTICLE INFO

Article history:
Received 14 January 2015
Received in revised form
16 June 2015
Accepted 2 July 2015
Available online 9 July 2015

Keywords:
Multi-cell tube
Oblique impact
Crashworthiness
Complex proportional assessment
Multiobjective optimization

ABSTRACT

Multi-cell tubes have been drawn increasing attention for their excellent energy-absorbing ability. However, the effect of cell number and oblique loads on crashing behaviors has seldom been studied to date. In this paper, a group of multi-cell tubes with different cell numbers were comprehensively investigated under both axial and oblique loads. The finite element models were first established and then validated by experimental tests. The simulation results showed that the increase in cell number can be beneficial to the energy absorption (*EA*) but detrimental due to increase in peak force (F_{max}) under axial load. When the oblique loads were taken into account, the tubes could undergo global bending, which is an inefficient deformation mode. By applying complex proportional assessment (COPRAS) method, the 7×7 tube was selected as the best based on multi-criteria under multiple loading angles. Then the Kriging modeling technique and multiobjective particle optimization (MOPSO) algorithm were integrated to address the optimization problems, where *EA* and F_{max} were taken as objectives and tube sizes as design variables. The results demonstrated that different loading angles have different requirements on cell allocation and optimizations of multiple load cases (MLC) can yield better solutions in a weighted average fashion, whereas the optimization for separate single load cases (SLC) could result in inferior performance under other load cases.

© 2015 Elsevier Ltd. All rights reserved.

1. Introduction

Thin-walled structures such as front longitudinal rails are widely used to dissipate the vehicle's kinetic energy in terms of plastic deformation in case of the frontal collision. To better understand axial crushing behaviors of thin-walled structures, substantial efforts have been made by using analytical, numerical and experimental methods. In this regard, Alexander [1] conducted the pioneering research on the axial crushing for thin cylindrical shells and derived an approximate analytical formulas for average crushing force. Later, substantial experimental and theoretical studies by Wierzbicki and Abramowicz [2], Abramowicz and Jones [3,4] and others were carried on the studies on the axial crushing of square and circular tubes subjected to static and dynamic loads. It is generally known that the number of angular elements (e.g. corner configuration) on a tube's cross-section largely affects the energy absorption and crashing behaviors [2,5]. For this reason, it is expected to design thin-walled tubes with multiple cells and internal webs for achieving better energy-absorbing characteristics. For example, Kim [6] proposed a new multi-cell tube with four square cells at the corners and found that this structure has dramatic improvement in energy absorption over the conventional square box column. Based on the super folding element theory, Zhang et al. [7] derived an analytical solution for the mean crushing force of multi-cell sections, which agrees well with the numerical results. Later, Alavi Nia and Parsapour [8] demonstrated that for a 3×3 cellular tube, adding the partitions at corners can enhance energy absorption and thereby corrected Zhang et al.'s formula of mean crushing load for multi-cell tubes with unequally sized compartment. To maximize the energy absorption and minimize the peak force, Hou et al. [9] used response surface method to perform the design optimizations for single, double, triple and quadruple cell sectional columns. Tang et al. [10] devised a circular multi-cell column and verified its superiority to conventional square structure. Zhang and Zhang [11] studied the quasi-static axial crushing experimentally and analytically for multi-cell stub columns with different sectional configurations.

In automotive engineering, the bumper system requires to endure a load with up to 30° loading angle to the longitudinal axis [12]. Under this condition, thin-walled structures always undergo a combined deformation of bending and axial crushing, rather than pure axial collapse that is designed as an efficient deformation mode for energy absorption. Due to the presence of global

* Corresponding author. Fax: +86 21 6958 9845.
** Corresponding author. Fax: +86 731 8882 2051.
E-mail addresses: fangjg87@gmail.com (J. Fang), sgy800@126.com (G. Sun).

http://dx.doi.org/10.1016/j.tws.2015.07.002
0263-8231/© 2015 Elsevier Ltd. All rights reserved.

bending, the energy absorption of thin-walled structures can be reduced dramatically. For this reason, oblique loading has to be considered in crashworthiness design. For this purpose, Han and Park [13] investigated the crush behavior of a square column subjected to oblique loads and found that the loading angle has considerable effect on deformation pattern from the axial buckling to global bending. Reyes et al. [12,14,15] studied the crashworthiness performance of hollow and foam-filled aluminum tubes under quasi-static oblique loads by using experimental and numerical methods. Zarei and Kröger [16] performed axial and oblique impact tests on empty and aluminum honeycomb filled square tubes and they observed a dramatic decrease in the first peak load during the oblique impact test. Tarlochan et al. [17] proposed a design process for the thin-walled structure subjected to both axial and oblique loads and they found that the hexagonal profile was a better choice for energy absorption application. Yang and Qi [18] developed an optimization procedure for design of the empty and foam-filled square columns under oblique loading and the results showed that compared with the foam-filled tubes, the empty column can behave better under oblique impact but worse under pure axial loading. And they also investigated the crashworthiness and lightweight design for conical tubes under oblique impact [19]. To the author's best knowledge, there have been very limited studies on multi-cell tubes by taking into account the oblique loads so far. Qi et al. [20] employed LS-DYNA to predict the crashing behaviors of four tubes with different cellular configurations under oblique loads, and they found that multi-cell tapered tube has the best crashworthiness performance. Song and Guo [21] found that the effectiveness of multi-cell configuration for improving tubes' energy absorption reduces as the load angle increases, and multi-cell tubes can even have worse performance if they collapse in global bending mode.

From the abovementioned studies, it is known that comprehensive comparison of the crashworthiness of multi-cell structures with different cell numbers remains under-studied thus far. Furthermore, how does the cell number affect the crashworthiness under oblique loads? How to select a multi-cell tube for optimizing its crashworthiness when both oblique and axial loads are presented? This study aims to address these issues. The remainder of this paper will be organized as follows. Section 2 introduces the finite element modeling of multi-cell tubes and its experimental validation. Section 3 describes complex proportional assessment theory. Section 4 studies the crashworthiness of multi-cells under oblique loads. Section 5 conducts multiobjective optimizations, followed by the conclusions in Section 6.

2. Numerical modeling

2.1. Finite element (FE) model

As shown in Fig. 1, the structures to be analyzed here comprise a group of thin-wall multi-cell square tubes with the same axial length of $L=200$ mm and the same width of $b=75$ mm subjected to oblique impact loading. These square tubes have different cell numbers (i.e., $N\times N=1\times 1,\ 2\times 2,\ 3\times 3,\ \ldots,\ 10\times 10$), and are assigned different thicknesses in order to investigate these tubes with the same mass (Fig. 1). As shown in Fig. 2, a rigid wall with a mass of 600 kg and an incident angle θ impacts on the top end of the tubes at an initial velocity of $v=15$ m/s. the bottom ends of the tube is attached to the fixed rigid ground.

In this study, the numerical models were developed using explicit non-linear finite element code LS-DYNA. The Belytschko-Lin-Tsay reduced integration shell elements with five integration points through the thickness were employed to model the tubes. Stiffness-based hourglass control was employed to avoid spurious zero energy deformation modes and reduced integration was used to avoid volumetric locking. The interfaces between the tube and rigid wall and between the tube and rigid ground were both modeled as an "automatic node to surface". "Automatic single surface" contact was also prescribed to the tube to avoid interpenetration during tube folding. For both static and dynamic friction, the friction coefficient of 0.2 was adopted for all contact conditions [10,22,23].

The tube was modeled through a piecewise linear elastic-plastic behavior with strain hardening (material model 24 in LS-DYNA). The thin wall material was aluminum alloy AA6063-O with the density=2700 kg/m^3, Poisson's ratio=0.3, and Young's modulus=70 GPa, initial yield stress=46.5 MPa and ultimate stress=103 MPa. The material model was considered insensitive

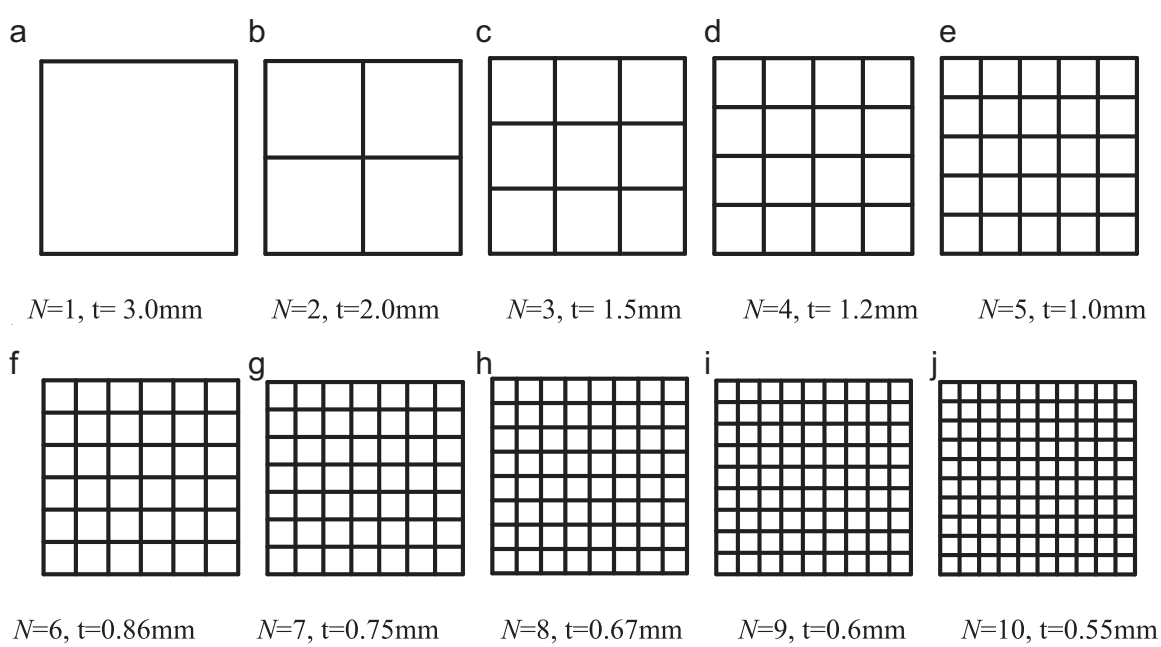

Fig. 1. Cross-sections of multi-cell tubes with the same mass but different wall thicknesses.

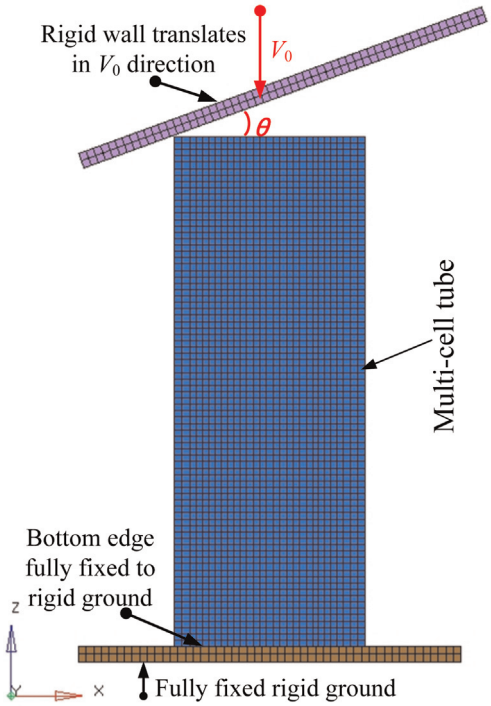

Fig. 2. Finite element model of multi-cell tube subjected to oblique loading.

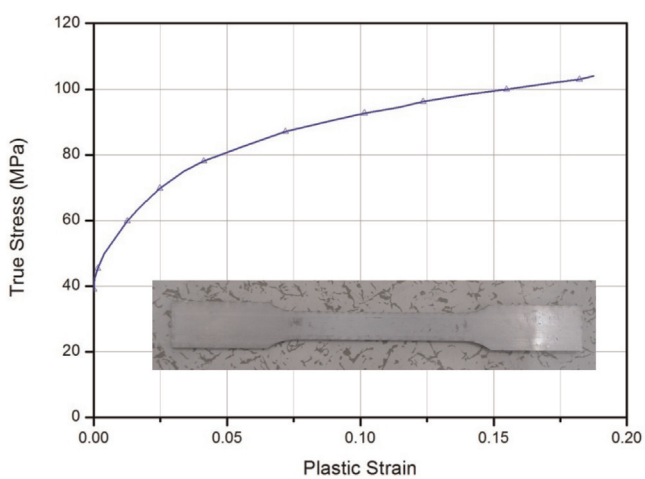

Fig. 3. Stress–strain curve.

to strain rate but defined as non-linear isotropic work hardening in the plastic region [24,25]. The obtained curve of stress versus strain by an in-house axial tensile test is provided in Fig. 3.

2.2. Validation of FE modeling

In order to decide the size of finite elements, a convergence test was carried out to minimize the effect of mesh size on the accuracy of numerical results. It is found that the optimal mesh size for the tubes is 2.5×2.5 mm^2, which was able to converge within a reasonable computing time and was used throughout the study.

In order to validate the FE modeling, a tube with 3×3 uniform cells was compressed using the available test facilities with a constant axial crush velocity of 3 mm/min (Fig. 4). The simulation model with the same specimen configuration was established under the same testing conditions. Fig. 5(a) depicts a comparison

Fig. 4. Experimental test for modeling validation.

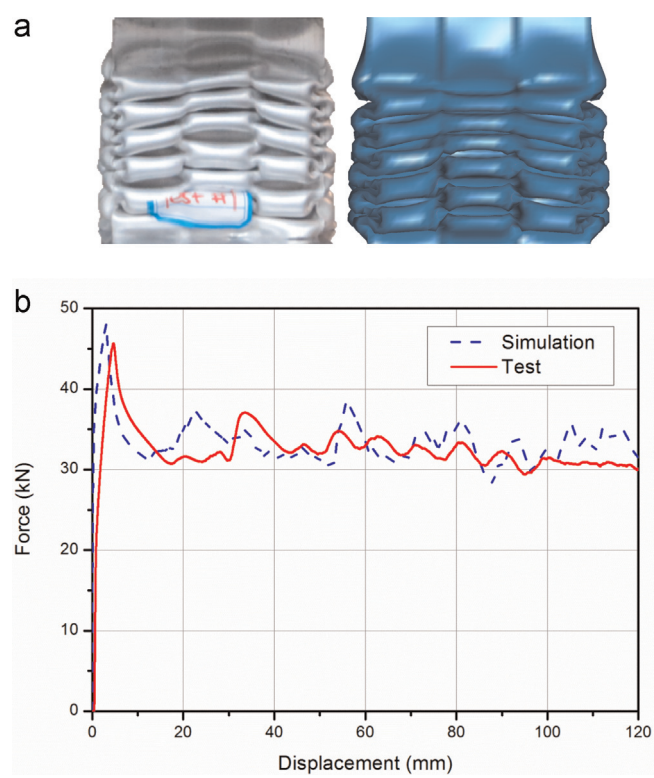

Fig. 5. Comparison of experimental and simulation results.

of the deformed shapes between the FE simulation and experimental tests. The overall profile of FE model in terms of the collapse mode and number of folds is in good agreement with the experiment. Fig. 5(b) illustrates a comparison of the FE and experimental results of the load–displacement responses, in which a fairly good overall agreement between them is observed. From which, it is easily found that the maximum discrepancy of initial peak force is less than 5% and the FE prediction exhibits a slightly higher peak load than the experiment during the subsequent folding. This could be attributed to that the existence of imperfections in the physical specimen, which is difficult to be considered precisely in FE modeling. Overall, the numerical modeling technique adopted here is considered sufficiently accurate and will be extended to the subsequent study.

To further validate the FEA results under dynamic oblique loading conditions, the mean crushing force for tube $N=3$ with $\theta=15^\circ$ was also compared with the theoretical solution. The theoretical solution of mean crushing force for multi-cell square tube under axial loading condition can be described as [26]:

$$F_{\text{axial}} = \frac{2}{k} M_0 \sqrt{\frac{2(N_c + 4N_o + 2N_T)\pi L_c}{t}} \tag{1}$$

where $M_0=(1/4)\sigma_0 t^2$ denotes the fully plastic bending moment per unit width, t represents the wall thickness. σ_0 Is the flow stress of the tube material, which can be calculated as the average of initial yield stress and ultimate stress. k Is the efficient crush length coefficient and is set to 0.8 herein [11]. N_c, N_o and N_T denote the number of corners, crisscrosses and T-shapes, respectively. L_c is the total length of the wall section. Obviously, for the tube with $N=3$ in this study, $N_c=4$, $N_o=4$, $N_T=8$ and $L_c=8b$. By substituting them into Eq. (1), the theoretical predition of mean crushing force is

$$F_{\text{axial}} = \frac{21.27}{k} \sigma_0 b^{0.5} t^{1.5} \tag{2}$$

The corresponding theoretical prediction of mean crushing force under oblique loads can be calculated as follows

$$F_{\text{oblique}} = \lambda \frac{21.27}{k} \sigma_0 b^{0.5} t^{1.5} \tag{3}$$

where oblique coefficient λ was introduced to take into account the geometry parameters, inertia effect and the loading angles, and could be calculated by the following equation [27].

$$\lambda = (10{*}t/b + 1.1){*}\ \cos\ \theta \tag{4}$$

In this study, theoretical prediction of mean crushing force for the multi-cell tube with $N=3$, $\theta=15^\circ$, $t=1.5$ mm and $b=75$ mm is 32.00 kN from Eq. (2). The FE result is 30.02 kN and thus the difference between FE and theoretical solution is 6.7%, which indicates that the FE result agrees fairly well with the theoretical prediction.

3. Complex proportional assessment methodology

This study involves selection of a tube with the best crashing behavior under axial and oblique loads, which belongs to a multicriteria decision-making (MCDM) problem. The preference ranking method of complex proportional assessment (COPRAS) developed by Zavadskas et al. [24] is adopted herein for this MCDM process for its simplicity in usage. It assumes direct and proportional dependences of significance and utility degree of the available alternatives under the presence of mutually conflicting criteria. The detailed procedure of applying the COPRAS method consists of the following steps:

Step 1: Prepare the decision-making matrix **X,** which maps the alternatives to the selection criteria.

$$\mathbf{X} = [x_{ij}]_{mn} = \begin{bmatrix} x_{11} & x_{12} & & x_{1n} \\ x_{21} & x_{22} & & x_{2n} \\ \cdots & \cdots & \cdots & \cdots \\ x_{m1} & x_{m2} & & x_{mn} \end{bmatrix} \tag{5}$$

where x_{ij} is the performance value of the ith alternative against the jth criterion, and m and n denote the number of alternatives and the number of criteria, respectively.

Step 2: Normalize the decision matrix using Eq. (5) to attain the non-dimensional values of different criteria so that all of them can be compared.

$$R = \left[r_{ij}\right]_{mn} = \frac{x_{ij}}{\sum_{i=1}^{m} x_{ij}} \tag{6}$$

Step 3: Identify the weight of each criterion using the following approach [17].

- Comparing every two criteria at a time, total comparison sets of $n(n-1)/2$ need to be considered. Taking three criteria ($n=3$) case as example, $3(3-1)/2=3$ comparison sets are required as shown in Table 1 (i.e., $F_{\max}$ vs. *EA*, $F_{\max}$ vs. *CFE*, and *EA* vs. *CFE*).
- For the two criteria being selected from the comparison sets, the more important criterion is given a score of three (3), whereas a score of one (1) is given to the less important criterion. If both criteria are of equal importance, they can have equal scores of two (2). Repeat this for other comparison sets. In Table 1, we focus more on $F_{\max}$ and *EA* and take CFE as the secondary criterion.
- Then the total score obtained for the jth criterion is computed as $\sum_{i=1}^{m} N_{ij} = W_j$.
- Obtain the weight of the jth criterion w_j by dividing the total score for each selection criterion W_j by the global total score $G = \sum_{i=1}^{n} W_j$.

Table 1
Example of weightage setting.

Selection criteria	Number of comparison sets (3(3−1)/2=3)			W_j	w_j
	1	2	3		
$F_{\max}$	2	3		5	5/12=0.417
EA	2		3	5	5/12=0.417
CFE		1	1	2	2/12=0.167

Step 4: Calculate the weighted normalized decision matrix D.

$$D = \left[y_{ij}\right]_{mn} = r_{ij} \times w_j \tag{7}$$

where r_{ij} is the normalized performance value of the ith alternative with the jth criterion, and w_j is the weight of the jth criterion.

Step 5: Sum up the weighted normalized values for both beneficial attributes and non-beneficial attributes. A low value of a non-beneficial attribute is preferred for selection, whereas a great value of a beneficial attribute is favorite. These sums are determined by the following equations:

$$S_{+i} = \sum_{i=1}^{m} y_{+ij} \tag{8}$$

$$S_{-i} = \sum_{i=1}^{m} y_{-ij} \tag{9}$$

where y_{+ij} and y_{-ij} are the weighted normalized values for the beneficial and non-beneficial attributes, respectively.

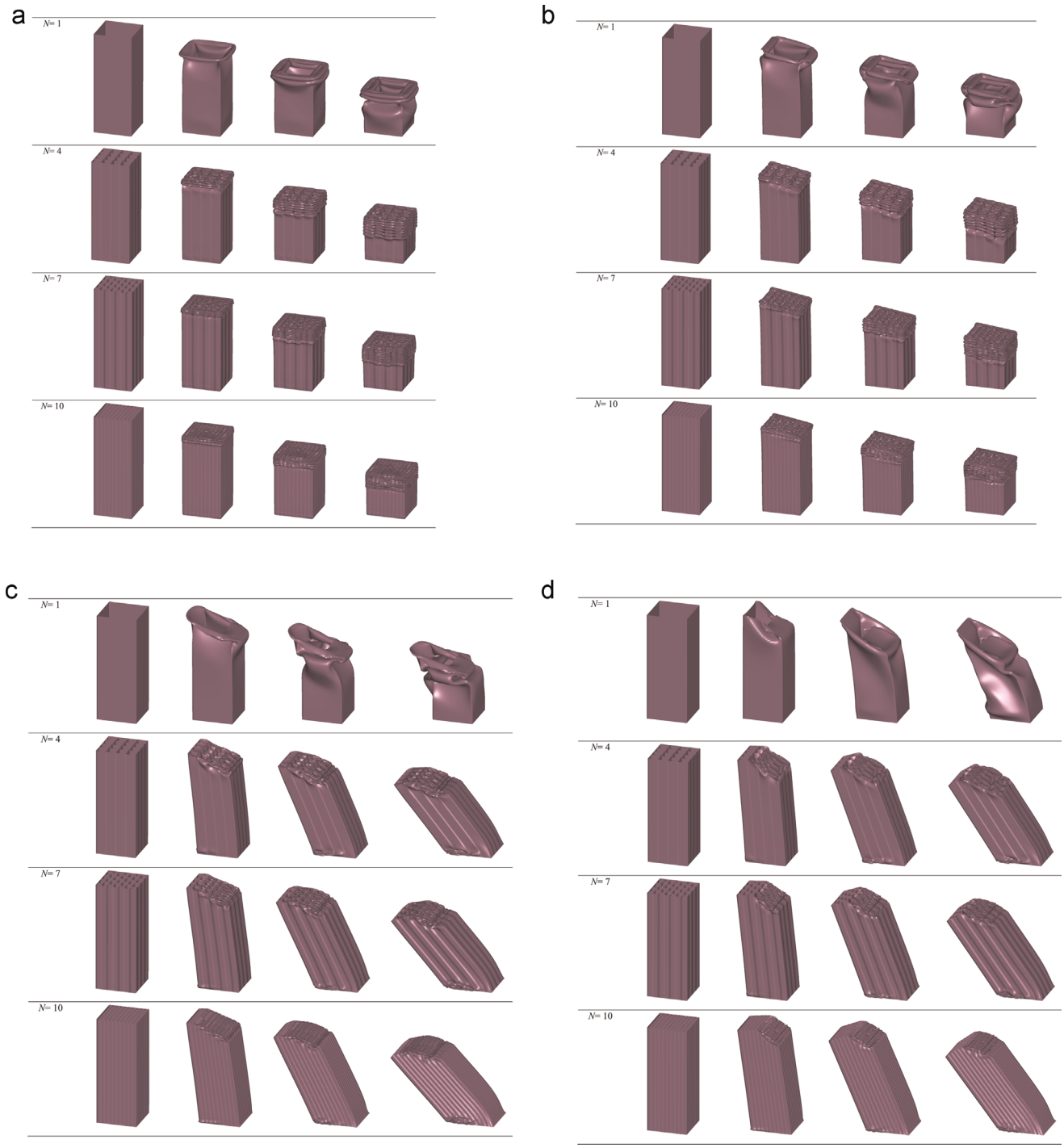

Fig. 6. Deformation modes of multi-cell tubes with different cell number N: (a) $\theta=0°$, (b) $\theta=10°$, (c) $\theta=20°$, and (d) $\theta= 30°$.

Step 6: Calculate the minimal value of S_{-i} as follows:

$$S_{-\min} = \min S_{-i} \tag{10}$$

Step 7: Determine the relative significance or priorities of an alternative. The priorities of the candidate alternatives are calculated based on the notion of relative significance Q_i. The relative significance value Q_i of the ith alternative can be formulated as below

$$Q_i = S_{+i} + \frac{S_{-\min} \sum_{i=1}^{m} S_{-i}}{S_{-i} \sum_{i=1}^{m} (S_{-\min}/S_{-i})} \tag{11}$$

Eq. (11) can be rewritten as

$$Q_i = S_{+i} + \frac{\sum_{i=1}^{m} S_{-i}}{S_{-i} \sum_{i=1}^{m} (1/S_{-i})} \tag{12}$$

Step 8: Calculate the quantitative utility U_i for the ith alternative. The degree of the quantitative utility, leading to a complete ranking of the alternatives, can be obtained by dividing the priority by the most efficient as

$$U_i = \frac{Q_i}{Q_{\max}} \times 100\% \tag{13}$$

where $Q_{\max}$ is the maximum relative significance value. The degree of the quantitative utility is directly proportional to the

relative significance and the quantitative utility with the value of 100 corresponds to the best design or candidate alternative using the method.

4. Crashworthiness of multi-cell tubes under different load angles

4.1. Crashworthiness criteria

To systematically measure the crashworthiness of different structures, many different indicators have been proposed [28–30], of which the energy absorption (*EA*) denotes the absorbed energy via plastic deformation of structures as

$$EA = \int_0^{\delta} F(\mathbf{x})dx \tag{14}$$

where $F(\mathbf{x})$ is the instantaneous crushing force in axial direction. δ denotes the crash displacement up to 0.6 L in this study, and $L=$ 200 mm is the tube length.

In addition to energy absorption, crushing forces designate other key crushing criteria, of which peak crushing force ($F_{\max}$) represents the maximum value of $F(\mathbf{x})$. The mean crushing force (MCF) measures the level of average crushing force as

$$F_{\text{avg}} = \frac{EA}{\delta} = \frac{\int_0^{\delta} F(\mathbf{x})dx}{\delta} \tag{15}$$

Besides, crushing force efficiency (*CFE*) is also used as an indicator given as

$$CFE = \frac{F_{\text{avg}}}{F_{\max}} \times 100\% \tag{16}$$

Note that a large $F_{\max}$ often leads to a high deceleration and high risk of severe injury or even death of occupant when impact occurs. Besides, the higher the *CFE* value, the better the load uniformity for an energy absorber. In this paper, these above-mentioned indictors will be considered under oblique and axial loads.

4.2. Results of pure axial crashing

Fig. 6a displays the progressive collapses of multi-cell tubes with the different cell numbers of 1×1, 4×4, 7×7 and 10×10 (i.e., $N=1$, 4, 7 and 10) under pure axial loads respectively, and Fig. 7a depicts the corresponding crushing force vs displacement curves. For the single cell structure ($N=1$), it can be seen that the crushing force first reaches an initial peak, followed by a dramatic drop and then fluctuates at some low values that correspond to the progressive folding. When cell number N increases, the crush force does not increase noticeably in the initial peak and tends to be stable during the whole crushing process. Specifically, the difference between the initial peak and the following peaks becomes small, and the force tends to fluctuate within a narrow range when cell number N increases. This might be attributed to that the fold length (the distance between two adjacent plastic hinges) decreases and thus the fold number increases with the increase in N (as shown in Fig. 6).

From Fig. 8(a) it can be seen that under the same mass the *EA* increases with the cell number, but the increased value become

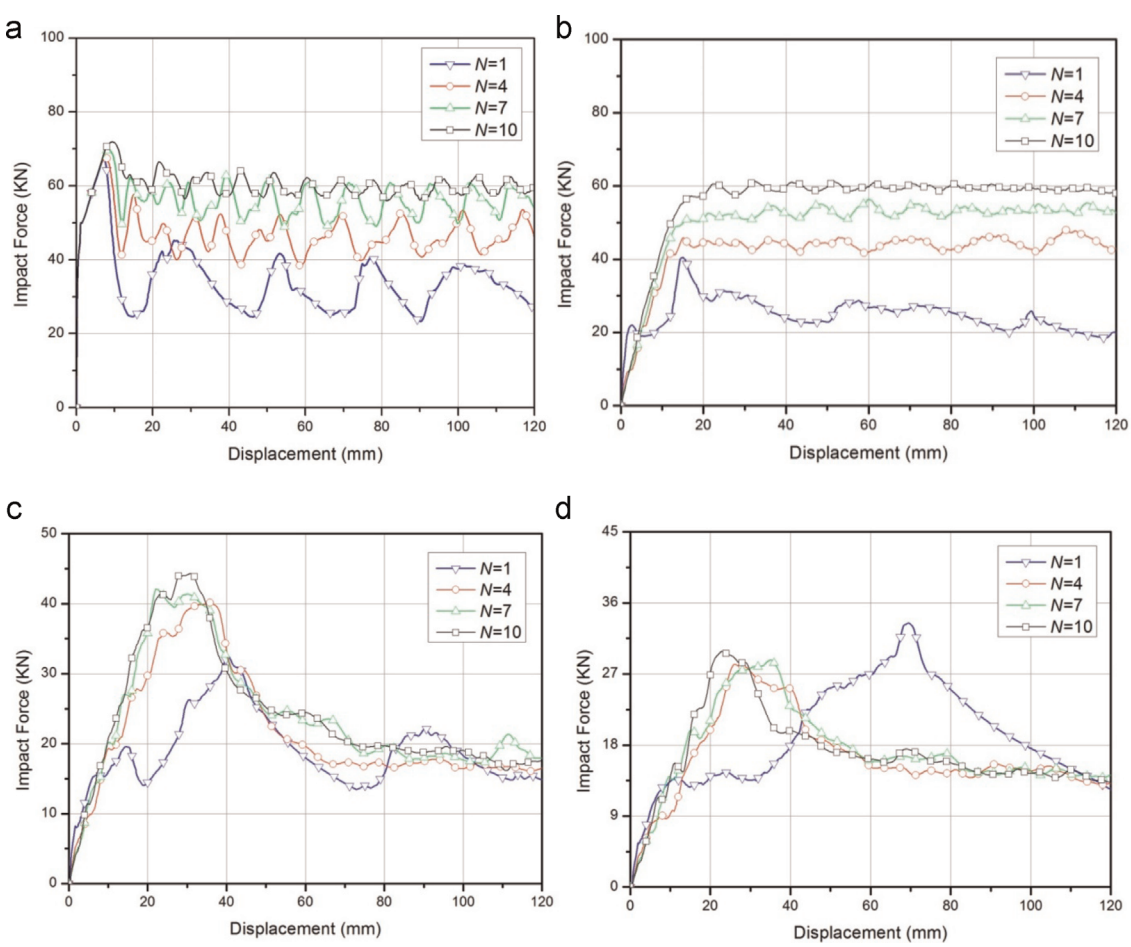

Fig. 7. Crashing force vs. displacement curve: (a) $\theta=0°$, (b) $\theta=10°$, (c) $\theta=20°$, (d) $\theta=30°$.

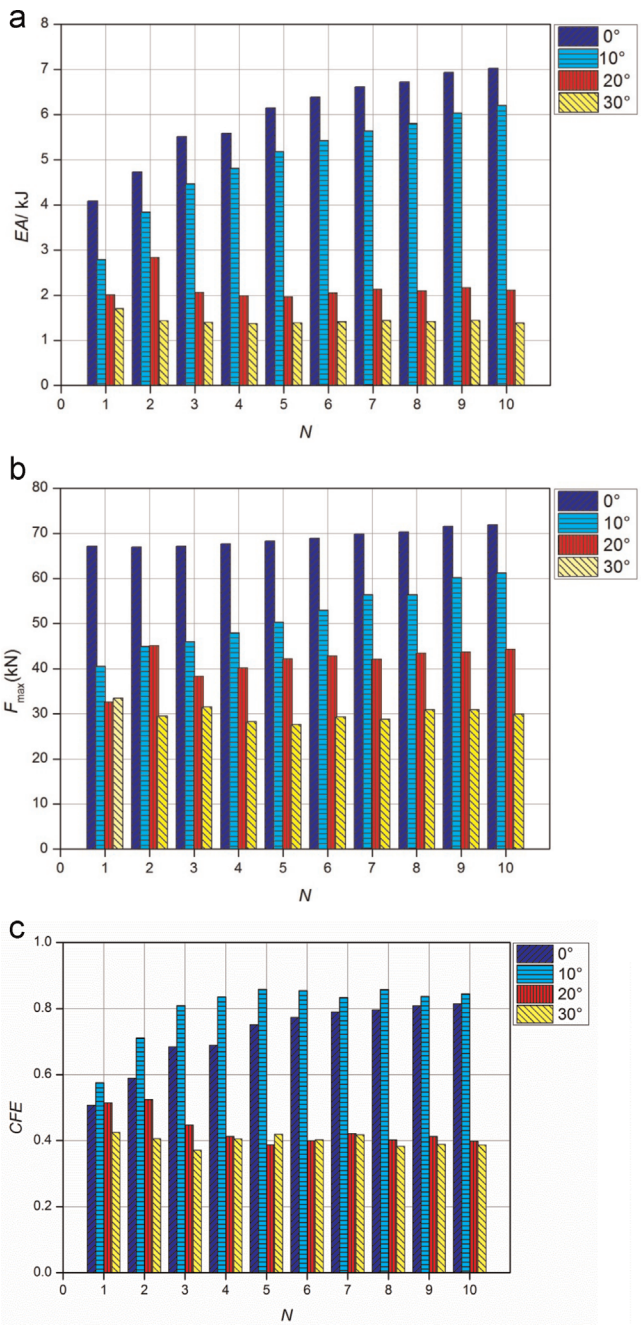

Fig. 8. Performance comparisons under different loading angles: (a) *EA*, (b) F_{max}, (c) *CFE*.

smaller and smaller, which imply that the energy absorption becomes stable gradually. From Fig. 8(b), the value of F_{max} increases fairly slowly when the cell number increases, indicating that F_{max} is insensitive to the cell number under the pure axial load condition. As for the *CFE*, its value increases when $N<4$ and then oscillates when $N>4$.

4.3. Results of oblique crashing

From Fig. 6(b), the deformation modes of tubes under the oblique impact of $\theta=10°$ are fairly similar to those of $\theta=0°$. That is to say that when the tubes are subjected to the oblique impact with a small incident angle, they are still able to generate proper progressive folding in the axial direction, which is typically regarded as an efficient deformation pattern. Interestingly, the impact forces fluctuate within a fairly small range after the initial peaks when θ increases from 0° to 10° (Fig. 7(b)). Similarly to the situations of $\theta=0°$, the more the cells of the tube has, the larger the force bears during the impact. As a result, it is observed from Fig. 8(a) and (b) that the increase in cell number N leads to the increase of F_{max} and *EA*. Besides, the F_{max} and *EA* of all tubes both decrease when θ increases from 0° to 10°; and the F_{max} decreases more than *EA* does, which well explains why the *CFE* of $\theta=10°$ is larger than that of $\theta=0°$ for each tube (Fig. 8(c)), since the *EA* is equivalent to F_{avg} (see Eq. (15)).

When θ increases to 20°, the global bending mode is observed for the tubes with more cells ($N>2$). The compression flange buckles and develops a plastic hinge close to the clamped distal end (in $N=4$, 7, 10 in Fig. 6(c)). Then the whole tube bends around this hinge as almost an rigid body motion. On the other hand, the tubes with a smaller cell number (e.g. $N=1$ and 2) still succeed to avoid such a global bending. From Fig. 7(c), the tubes of $N=4$, 7 and 10 reach a peak load and then decrease dramatically due to the global bending, weakening the energy absorption and load-carrying capacity. As a result, Fig. 8a and b exhibit that the *EA* and F_{max} of $N=4$, 7 and 10 reduce much more when θ increases from 10° to 20°, compared with those of $N=1$ and 2. When θ increases up to 30°, global buckling occurs in all the tubes (Fig. 6(d)) and the *EA* and F_{max} become even smaller (as Fig. 8(a) and (b)). Interestingly, from Fig. 7(d), the tube of $N=1$ undergoes a longer deformation before the impact force decreases significantly, representing that it bends later than the other three.

Overall, when multi-cell tubes are impacted obliquely with a small loading angle θ, all of them collapse progressively in the axial direction, which is very similar to the situation in the pure axial loading. When θ increases, multi-cell tubes begin to bend globally, which leads to reduction of load-carrying and energy absorption. It can also be seen that the tubes with more cells are more sensitive to oblique loads, although they can absorb more energy in pure axial case and oblique case with a small angle θ.

4.4. Selection of the cell number

In this section, we will use the complex proportional assessment (COPRAS) method to select the best tube for such a specific multi-criteria decision-making (MCDM) problem. The *EA*, F_{max} and *CFE* at each loading angle are considered as the criteria for selecting the most suitable one from these 10 multi-cell tubes. Of these criteria, *EA* and *CFE* are beneficial attributes where greater values are desirable, while F_{max} are non-beneficial attributes where smaller value is preferable. We consider 4 different impacting angles for each of these criteria. For all these different multi-cell tubes, 10 candidate alternatives are considered. Thus, the decision matrix of this MCDM problem consists of 10 tubes and 12 crashworthiness criteria, as shown in Table 2.

In this study, it is assumed that the indicators at different loading angles are considered equally important, and the *EA* and F_{max} play more critical roles than *CFE* as they directly reflect the crashworthiness. Following the procedure of Step 4 in Section 3, the weight factors for *EA*, F_{max} and *CFE* of each loading angle are identified as 0.09848, 0.09848 and 0.05303, respectively. The decision matrix as shown in Table 2 is normalized using Eq. (6) and the corresponding weighted normalized decision matrix is established in Table 3. Then, using Eqs. (8) and (9), the sums of the weighted normalized values are calculated for both beneficial attributes and non-beneficial attributes as given in Table 4. By applying Eq. (12), the relative significance or priority value (Q_i) for each alternative cell number is thus determined. Table 4 also exhibits the value of quantitative utility (U_i) for each alternative on the basis of which the complete ranking of the alternative tubes is obtained. The COPRAS result shows that the tubes with more cells

Table 2
Decision matrix.

N		1	2	3	4	5	6	7	8	9	10
0°	F_{max}	67.08	66.96	67.12	67.62	68.24	68.88	69.87	70.35	71.53	71.91
	EA	4.08	4.73	5.51	5.59	6.15	6.39	6.62	6.72	6.93	7.02
	CLE	0.51	0.59	0.68	0.69	0.75	0.77	0.79	0.80	0.81	0.81
10°	F_{max}	40.49	44.95	46.01	47.95	50.28	52.94	56.37	56.35	60.14	61.21
	EA	2.79	3.84	4.46	4.81	5.18	5.43	5.64	5.80	6.04	6.20
	CLE	0.58	0.71	0.81	0.84	0.86	0.85	0.83	0.86	0.84	0.84
20°	F_{max}	32.53	45.06	38.31	40.16	42.19	42.84	42.10	43.38	43.72	44.30
	EA	2.01	2.84	2.06	1.99	1.96	2.05	2.13	2.09	2.16	2.11
	CLE	0.51	0.52	0.45	0.41	0.39	0.40	0.42	0.40	0.41	0.40
30°	F_{max}	33.46	29.51	31.52	28.22	27.68	29.33	28.77	30.92	30.93	29.89
	EA	1.71	1.44	1.40	1.37	1.39	1.42	1.44	1.42	1.44	1.39
	CLE	0.42	0.41	0.37	0.41	0.42	0.40	0.42	0.38	0.39	0.39

generally perform better than those with fewer cells, but when too many cells are involved, the wall thickness becomes overly small and adversely affects the performance. Thus the best choice of tube under multiple load angles is the multi-cell tube with $N=7$, which will be optimized further in the following section.

Note that this "best" configuration may be only valid for the specific geometrical and material properties of the tubes chosen, as well as the specified loading and boundary conditions. In other words, when these factors change the best configuration could change. Therefore, the engineer should use COPRAS to re-make the decision for each specific case rather than assume that there is one configuration suitable to all other cases.

5. Multiobjective optimization of crashworthiness

5.1. Definition of optimization problem

An optimal structure is expected to have the maximum overall performance under different load cases [20,31–34]. In the present study, multiple load cases (MLC) in terms of different loading angles (θ) will be considered. For this reason, a weighted average criterion is formulated here as [20]

$$\begin{cases} F_{\max,\lambda} = \sum_{i=1}^{k} F_{\max,i}\lambda_i \\ EA_{\lambda} = \sum_{i=1}^{k} EA_i\lambda_i \end{cases} \tag{17}$$

where k denotes the number of load cases considered ($k=4$ herein), $F_{max,1}$, $F_{max,2}$, $F_{max,3}$ and $F_{max,4}$ represent the values of F_{max} at the loading angle $\theta=0°$, 10°, 20° and 30°, respectively. EA_1, EA_2, EA_3 and EA_4 denote the corresponding values of *EA*. Obviously, the weighting factor λ_i reflects the relative importance of individual $F_{max,i}$ and EA_i. Typically, the weighting factors are normalized as follows:

$$\sum_{i=1}^{k} \lambda_i = 1, \quad \lambda_i \geq 0 \tag{18}$$

It has proven that the cell size could affect the tube's crashing behaviors significantly [8]. While the best number of tube cells has been identified as $N=7$, the issue remains to be addressed is how to further optimize the cell sizes. Thus, we formulate the following optimization problem for each loading angle θ, in which the cell sizes (in terms of x_1, x_2 and x_3) are regarded as the design variables and $F_{\max,\lambda}$ and EA_{λ} as the objectives.

Table 3
Normalized decision matrix.

N		1	2	3	4	5	6	7	8	9	10
0°	F_{max}	0.0973	0.0971	0.0973	0.0981	0.0990	0.0999	0.1013	0.1020	0.1037	0.1043
	EA	0.0683	0.0792	0.0923	0.0935	0.1029	0.1070	0.1108	0.1125	0.1161	0.1175
	CFE	0.0704	0.0818	0.0951	0.0956	0.1043	0.1074	0.1096	0.1105	0.1122	0.1130
10°	F_{max}	0.0784	0.0870	0.0890	0.0928	0.0973	0.1025	0.1091	0.1091	0.1164	0.1185
	EA	0.0557	0.0764	0.0890	0.0958	0.1032	0.1081	0.1123	0.1156	0.1203	0.1236
	CFE	0.0718	0.0887	0.1009	0.1042	0.1071	0.1066	0.1039	0.1070	0.1044	0.1053
20°	F_{max}	0.0785	0.1087	0.0924	0.0969	0.1018	0.1033	0.1015	0.1046	0.1055	0.1068
	EA	0.0939	0.1325	0.0961	0.0929	0.0916	0.0959	0.0994	0.0978	0.1011	0.0988
	CFE	0.1191	0.1215	0.1036	0.0955	0.0897	0.0925	0.0975	0.0931	0.0954	0.0921
30°	F_{max}	0.1114	0.0983	0.1050	0.0940	0.0922	0.0977	0.0958	0.1030	0.1030	0.0996
	EA	0.1183	0.0997	0.0972	0.0953	0.0965	0.0982	0.1000	0.0985	0.1000	0.0962
	CFE	0.1061	0.1014	0.0926	0.1013	0.1047	0.1005	0.1043	0.0956	0.0971	0.0966

Table 4
Result of COPRAS.

N	1	2	3	4	5	6	7	8	9	10
S_+	0.0526	0.0591	0.0577	0.0582	0.0603	0.0619	0.0636	0.0633	0.0648	0.0645
S_-	0.0360	0.0385	0.0378	0.0376	0.0384	0.0397	0.0402	0.0412	0.0422	0.0423
Q_i	0.0956	0.0993	0.0986	0.0994	0.1006	0.1008	0.1022	0.1009	0.1015	0.1012
U_i	93.55%	97.13%	96.53%	97.26%	98.47%	98.69%	100.00%	98.72%	99.29%	99.00%
Rank	10	8	9	7	6	5	1	4	2	3

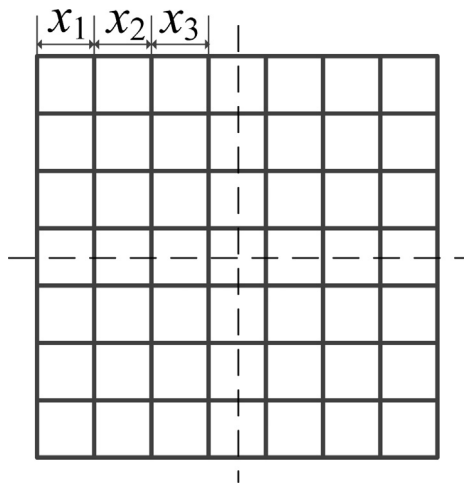

Fig. 9. Design variables.

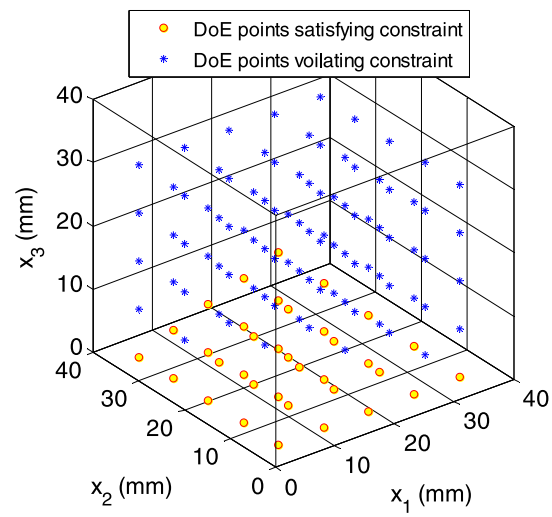

Fig. 10. DoE sample points.

$$\begin{cases} \min\left\{F_{\max,\lambda}(\mathbf{x}),\ -EA_{\lambda}(\mathbf{x})\right\} \\ \text{s.t.}\mathbf{x} = [x_1, x_2, x_3]^T \geq [2, 2, 2]^T \\ 37.5-(x_1 + x_2 + x_3) \geq 1 \end{cases} \tag{19}$$

Due to the symmetry, three design variables are selected as shown in Fig. 9. The constraints are set by considering the cell size limit (2 mm herein to avoid overlap across the wall thickness).

5.2. Kriging model and optimization algorithm

Since the crashworthiness problem of the multi-cell structure is highly nonlinear and complicated, direct coupling of optimization algorithm with simulation model may not be efficient (if not impossible). As an alternative, the meta- or surrogate modeling techniques have proven effective to replace full simulations for the optimization [35–38]. The surrogate model can provide an approximate functional relationship by relating design variables to specific objective with a moderate number of full computational analyses. In this regard, the Kriging model has exhibited a fairly good accuracy for highly nonlinear design problems [24,39–41] and will be employed to construct the surrogate models for crashworthiness objectives in this paper.

The Kriging model was originally developed for mining and geostatistical applications involving spatially and temporally correlated data [42]. The Kriging model assumes the deterministic response of a system to be a stochastic process function $y(x)$, consisting of a regression model and a stochastic error

$$y(\mathbf{x}) = \mathbf{f}(\mathbf{x})^T\boldsymbol{\beta} + z(\mathbf{x}) \tag{20}$$

where $\boldsymbol{\beta} = \left[\beta_1, \beta_2, \ldots, \beta_p\right]^T$ is the vector of regression parameters, $\mathbf{f}(\mathbf{x}) = \left[f_1(\mathbf{x}), f_2(\mathbf{x}), \ldots, f_p(\mathbf{x})\right]^T$ is the vector of basis functions; p denotes the number of basis functions; $z(\mathbf{x})$ represents a stochastic parameter with zero mean, variance σ^2, and nonzero covariance.

In this study, the full factorial design was adopted to generate sample points over the design space (Fig. 10). Note that the design points were filtered prior to the simulations, as only 35 of them can satisfy the constraints in Eq. (19). The 35 models were calculated to predict their crashworthiness performances under each load case. After that, the Kriging modeling technique was utilized to fit the objective functions in Eq. (19).

To examine the accuracy of surrogate modeling, five extra validation points yielded randomly in the design space were used to assess the relative error (R_e) of the established Kriging models as.

$$R_e = \left|\frac{f_{fea}(\mathbf{x}) - f_{krg}(\mathbf{x})}{f_{fea}(\mathbf{x})}\right| \tag{21}$$

where $f_{fea}(\mathbf{x})$ and $f_{krg}(\mathbf{x})$ are the solutions from the FEA and Kriging model at those validation points. The accuracy assessment results are displayed in Fig. 11. It can be seen that all the Kriging models can predict the responses with fairly small errors < 5%, making us confident to perform the optimizations by using the Kriging models.

To address the optimization problem defined in Eq. (19), multiobjective particle swarm optimization (MOPSO) algorithm is implemented. Particle swarm optimization (PSO) algorithm is a relatively new heuristic algorithm inspired by the choreography of a bird flock [43]. As an extended version to PSO, MOPSO is characterized by fast convergence and well-distributed Pareto frontier compared with other multiobjective optimization algorithms such as NSGA-II [44], PEAS and microGA etc. [45,46]. It is noted that MOPSO has been employed successfully to solve a series of design problems in sheet metal forming [47] and crashworthiness for functionally graded foam-filled structures [29]. In this paper, the MOPSO proposed by Coello et al. [45] is utilized to produce Pareto frontiers for the optimization problems of multi-cell tubes.

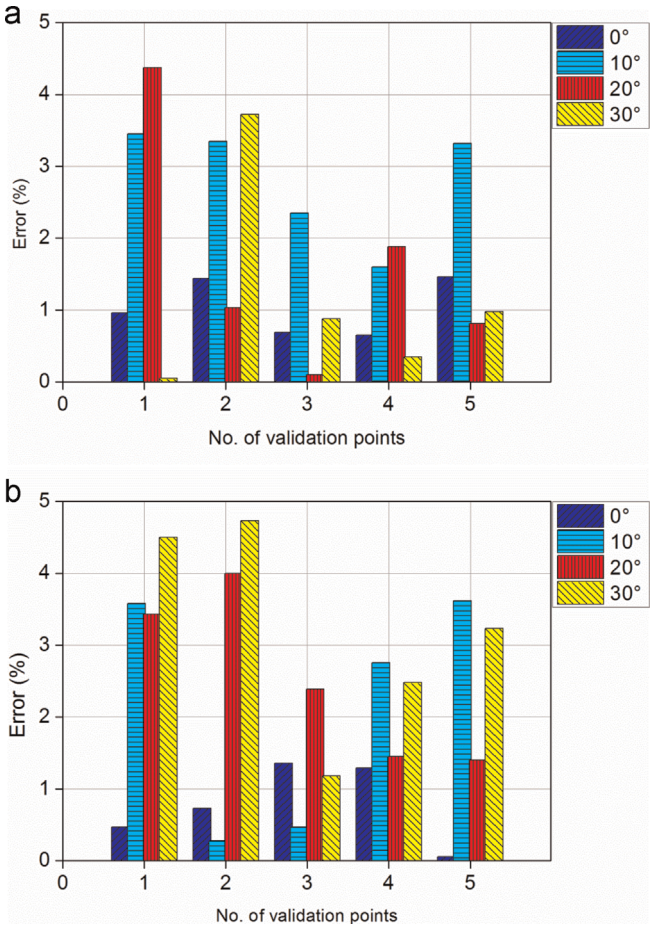

Fig. 11. Accuracy assessment of Kriging models: (a) *EA*, (b) F_{max}.

5.3. Optimization for different loading angles

In order to conduct optimizations for four different single load cases (SLC), where only one loading angle is considered in each case, we set the weighting factors as follows:

Case I ($\theta=0°$): $\lambda_1=1.0$, $\lambda_2=0.0$, $\lambda_3=0.0$, $\lambda_4=0.0$
Case II ($\theta=10°$): $\lambda_1=0.0$, $\lambda_2=1.0$, $\lambda_3=0.0$, $\lambda_4=0.0$
Case III ($\theta=20°$): $\lambda_1=0.0$, $\lambda_2=0.0$, $\lambda_3=1.0$, $\lambda_4=0.0$
Case IV ($\theta=30°$): $\lambda_1=0.0$, $\lambda_2=0.0$, $\lambda_3=0.0$, $\lambda_4=1.0$

In this problem, we iteratively check the accuracy of Pareto solutions and update the Kriging models until the Pareto frontiers become stable [48–51]. The converged Pareto frontiers for optimization problems of individual angle of $\theta=0$, 10, 20 and 30° are plotted together in Fig. 12. For each Pareto frontier, it is observed that F_{max} and *EA* conflict with each other and any improvement in one of the objectives must worsen the other, i.e., decrease in F_{max} always leads to undesirable decrease in *EA* or increase in *EA* results in unfavorable increase in F_{max}. In practice, the trade-off should be made between these two performances. Furthermore, when θ increases, the Pareto frontier moves up and left, representing the decrease in the optimum of F_{max} and *EA*. Also the *EA* range shrinks when θ increases up to 20° and 30°.

We adopt the minimum distance selection method (MDSM) [52] to select an overall optimum (namely knee point), and the result is also displayed in Fig. 12. Interestingly, when the tube is subjected to the pure axial load, the optimal internal ribs concentrate on the middle region. On the other hand, the internal ribs move outwards subjected to the oblique loads. This is probably because that the more ribs close to sides can enhance the resistance of the bending deformation, and thus improve the crashworthiness performances.

5.4. Optimization for multiple loading angles

Although the above SLC optimizations provide separate designs for each impact angle, they might offer undesirable designs for other loading case. For this reason, the weighting factor method is adopted to take into account multiple loading cases (MLC) in the optimization. The weighting factors define the relative importance (or accidental frequency) of each loading case to the overall crashworthiness. To investigate the effect of weighting factors on the optimization results, the following three design cases are considered to emphasize different loading angles:

Case I: $w_1=0.10$, $w_2=0.20$, $w_3=0.30$, $w_4=0.40$
Case II: $w_1=0.25$, $w_2=0.25$, $w_3=0.25$, $w_4=0.25$
Case III: $w_1=0.40$, $w_2=0.30$, $w_3=0.20$, $w_4=0.10$

Fig. 13 depicts the MCL Pareto frontiers of these three different design cases. The Pareto frontier moves down and right from Case I to Case III. This is because that from Case I to Case III, more importance is given to the loads of smaller angles (i.e., 0° and 10°) and optimizations under the smaller angles offer the designs with larger F_{max} and *EA* (as shown in Fig. 12).

Fig. 14a to d plot the optimums of the three MLC together with the four SLC designs in separate objective spaces. For each load

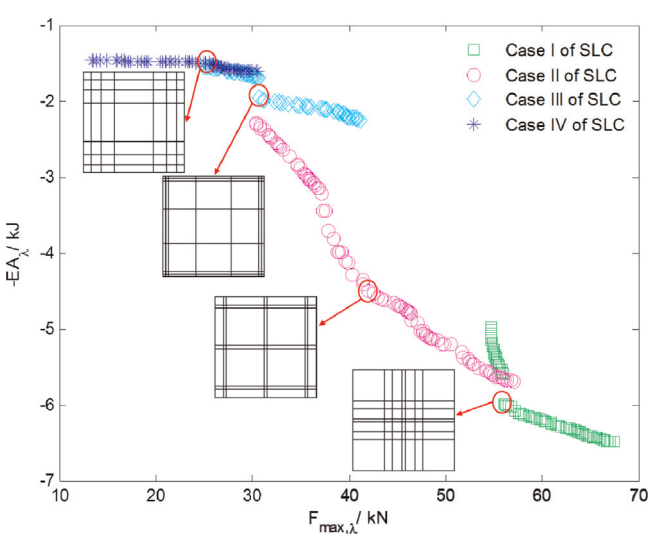

Fig. 12. Pareto frontiers for different single load cases (SLC).

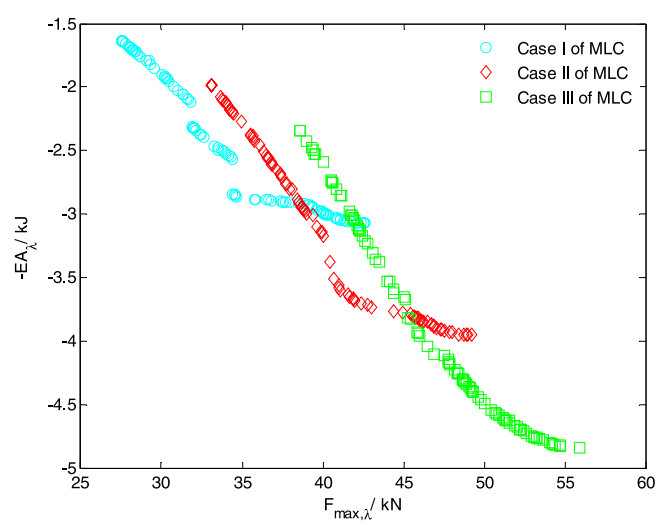

Fig. 13. Pareto frontiers for multiple loading case (MLC).

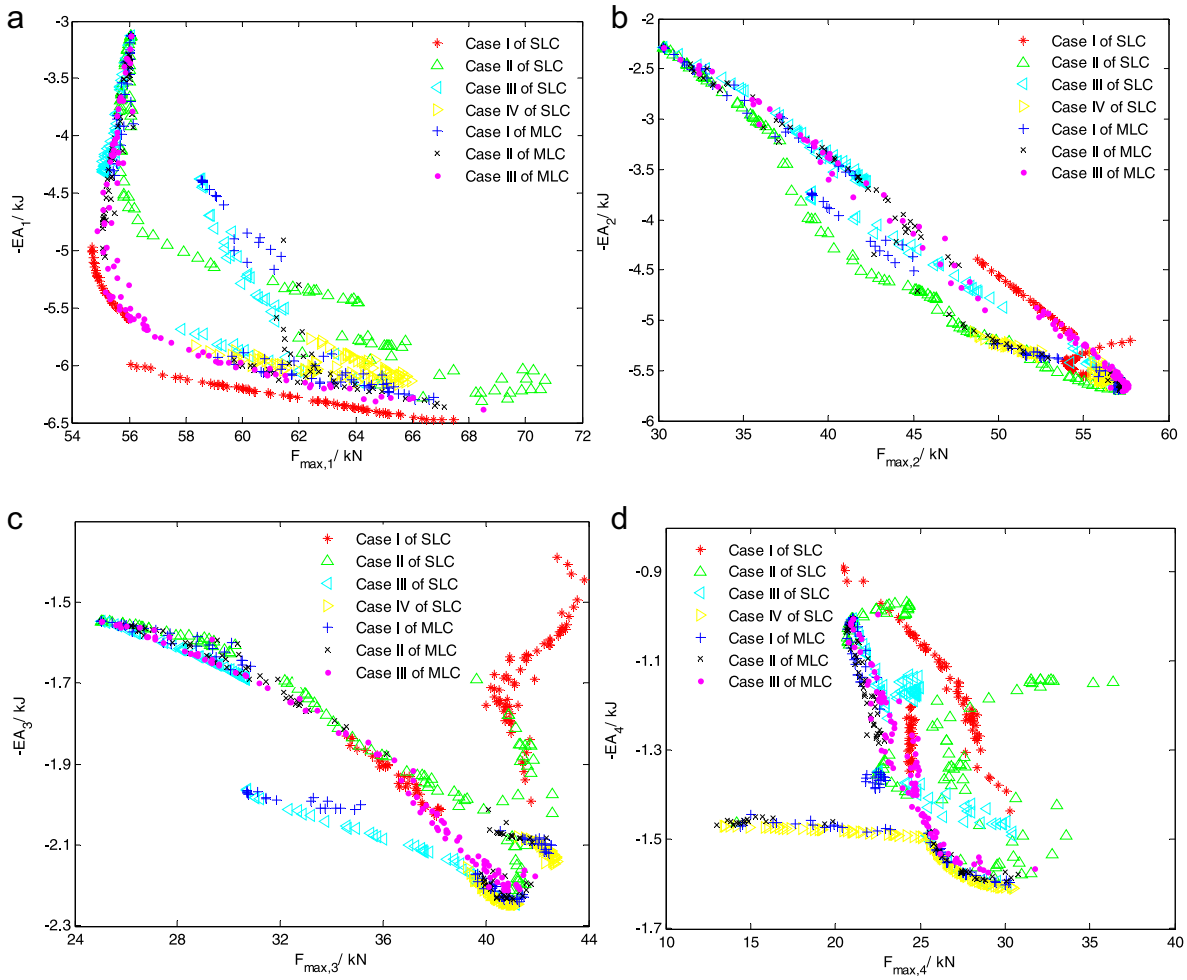

Fig. 14. Pareto solutions in objective spaces of each load case: (a) $\theta=0°$, (b) $\theta=10°$, (c) $\theta=20°$, (d) $\theta=30°$.

case, the corresponding SLC designs always outperform the MLC counterparts. In other words, if we consider the crashworthiness only for a specific load, SLC designs are able to inrease *EA* without enlarging F_{max}, or to lower F_{max} without sacrificing *EA* compared to the MLC designs. However, a SLC design that only considers a specific impacting anlge can considerably deteriorate the performances when the tube is subjected to other loading angles. For instance, Pareto optimal solutions for Case I of SLC, which only considers pure axial loads, could result in worse F_{max} and *EA* values under oblique loads. On the other hand, although MLC designs cannot obtain the best solutions for a specific load case, they help generate best possible solutions for all load cases in a weighted average fashion [31–33].

From Fig. 14a, moreover, Case III of MLC produces optimal solutions very close to the SLC solutions with $\theta=0°$ in the objective space, whereas the other cases obtain the solutions relatively far away. Similarly, from Fig. 14d the optimal solutions for Case I of MLC approach the SLC's with $\theta=30°$ whilst optimal solutions for the other cases are located in distant areas. As for Case II of MLC, however, this trend cannot be observed. This is because that Case III of MLC focuses the most on the loading case of $\theta=0°$ ($w_1=0.40$) and Case I of MLC emphasizes most on the loading case of $\theta=30°$ ($w_4=0.40$), whereas Case II of MLC places equal weighting to each loading angle.

From the above analyses, the weighting factors are of considerable importance to the final optimal results. Note that the weighting factors need to be determined properly, for example from statistical data about occurrence probablity or frequency of different loading scenarios, which is howvere beyond the scope of this study.

This study tried to address the optimization of mulcti-cell tubes involving both topological configuration (the cell number) and size variables. In fact, the ideal way to address this problem is performing size optimizations for each topological configuration. However, it could be rather expensive computationally and prohibited for real-life applications. Alternatively, a two-stage procedure (i.e. selection and optimization) was proposed to properly seek the optimum design, although it neglect the coupling effect between the two stages.

6. Conclusions

In this study, the crashing behaviors of multi-cell tubes with ten different cell numbers were comprehensively investigated under both axial and oblique loads. The simulation models were established using non-linear finite element code LS-DYNA and then validated by experimental test. It was found that both energy absorption (*EA*) and peak force (F_{max}) of multi-cell tubes increase with cell number under axial loads. Regarding the oblique loads, the tubes can remain to collapse progressively in axial direction when the incident angle (θ) is small, but they develop global bending when θ increases up to 20° and 30°. It was also observed that the tubes with fewer cells are more robust to oblique loads with large angle but perform worse under pure axial load than the tubes with more cells. The complex proportional assessment

(COPRAS) method was applied to this multi-criteria decision making exercise, and the results showed that considering both axial and oblique loads, the tubes with more cells are more competent and $N=7$ is selected as the best one herein. Following such optimal selection, a multiobjective optimization algorithm was adopted for the design of cell size, where energy absorption *EA* and F_{max} were taken as the objectives and cell sizes regarded as the design variables. The results demonstrated that the optimal solutions only considering separate load case (SLC) could lead to undesirable designs in other load cases. From the knee points, the internal ribs moves from the middle to the sides when the loading direction varies from axial to more oblique. The weighting factors are of considerable significance to the Pareto frontier of optimization of multiple load cases (MLC), and the MLC designs can help achieve more competent solutions when every load case is considered.

Acknowledgment

This work was supported from The National 973 Project of China (2011CB711205), The National Natural Science Foundation of China (11202072), The Hunan Provincial Science Foundation of China (13JJ4036), The Doctoral Fund of Ministry of Education of China (20120161120005) for providing financial support. The first author is a recipient of the doctoral scholarships from both China Scholarship Council (CSC) and the University of Sydney.

References

[1] J. Alexander, An approximate analysis of the collapse of thin cylindrical shells under axial loading, Q. J. Mech. Appl. Math. 13 (1960) 10–15.
[2] T. Wierzbicki, W. Abramowicz, On the crushing mechanics of thin-walled structures, J. Appl. Mech.-T Asme 50 (1983) 727–734.
[3] W. Abramowicz, N. Jones, Dynamic axial crushing of square tubes, Int. J. Impact Eng. 2 (1984) 179–208.
[4] W. Abramowicz, N. Jones, Dynamic progressive buckling of circular and square tubes, Int. J. Impact Eng. 4 (1986) 243–270.
[5] W. Abramowicz, T. Wierzbicki, Axial crushing of multicorner sheet metal columns, J. Appl. Mech. 56 (1989) 113–120.
[6] H.S. Kim, New extruded multi-cell aluminum profile for maximum crash energy absorption and weight efficiency, Thin-Walled Struct. 40 (2002) 311–327.
[7] X. Zhang, G.D. Cheng, H. Zhang, Theoretical prediction and numerical simulation of multi-cell square thin-walled structures, Thin Wall Struct. 44 (2006) 1185–1191.
[8] A. Alavi Nia, M. Parsapour, An investigation on the energy absorption characteristics of multi-cell square tubes, Thin Wall Struct. 68 (2013) 26–34.
[9] S.J. Hou, Q. Li, S.Y. Long, X.J. Yanga, W. Li, Multiobjective optimization of multi-cell sections for the crashworthiness design, Int. J. Impact Eng. 35 (2008) 1355–1367.
[10] Z. Tang, S. Liu, Z. Zhang, Analysis of energy absorption characteristics of cylindrical multi-cell columns, Thin Wall Struct. 62 (2013) 75–84.
[11] X. Zhang, H. Zhang, Energy absorption of multi-cell stub columns under axial compression, Thin Wall Struct. 68 (2013) 156–163.
[12] A. Reyes, M. Langseth, O. Hopperstad, Crashworthiness of aluminum extrusions subjected to oblique loading: experiments and numerical analyses, Int. J. Mech. Sci. 44 (2002) 1965–1984.
[13] D. Han, S. Park, Collapse behavior of square thin-walled columns subjected to oblique loads, Thin Wall Struct. 35 (1999) 167–184.
[14] A. Reyes, M. Langseth, O. Hopperstad, Square aluminum tubes subjected to oblique loading, Int. J. Impact Eng. 28 (2003) 1077–1106.
[15] A. Reyes, O. Hopperstad, M. Langseth, Aluminum foam-filled extrusions subjected to oblique loading: experimental and numerical study, Int. J. Solids Struct. 41 (2004) 1645–1675.
[16] H. Zarei, M. Kröger, Optimum honeycomb filled crash absorber design, Mater. Des. 29 (2008) 193–204.
[17] F. Tarlochan, F. Samer, A.M.S. Hamouda, S. Ramesh, K. Khalid, Design of thin wall structures for energy absorption applications: enhancement of crashworthiness due to axial and oblique impact forces, Thin Wall Struct. 71 (2013) 7–17.
[18] S. Yang, C. Qi, Multiobjective optimization for empty and foam-filled square columns under oblique impact loading, Int. J. Impact Eng 54 (2013) 177–191.
[19] C. Qi, S. Yang, Crashworthiness and lightweight optimisation of thin-walled conical tubes subjectedto an oblique impact, Int. J. Crashworthiness 19 (2014) 334–351.
[20] C. Qi, S. Yang, F.L. Dong, Crushing analysis and multiobjective crashworthiness optimization of tapered square tubes under oblique impact loading, Thin Wall Struct. 59 (2012) 103–119.
[21] J. Song, F.L. Guo, A comparative study on the windowed and multi-cell square tubes under axial and oblique loading, Thin Wall Struct. 66 (2013) 9–14.
[22] H.F. Yin, G.L. Wen, Z.B. Liu, Q.X. Qing, Crashworthiness optimization design for foam-filled multi-cell thin-walled structures, Thin Wall Struct. 75 (2014) 8–17.
[23] Z. Zhang, S. Liu, Z. Tang, Crashworthiness investigation of kagome honeycomb sandwich cylindrical column under axial crushing loads, Thin Wall Struct. 48 (2010) 9–18.
[24] J. Fang, Y. Gao, G. Sun, Y. Zhang, Q. Li, Parametric analysis and multiobjective optimization for functionally graded foam-filled thin-wall tube under lateral impact, Comput. Mater. Sci. 90 (2014) 265–275.
[25] J. Fang, Y. Gao, G. Sun, Y. Zhang, Q. Li, Crashworthiness design of foam-filled bitubal structures with uncertainty, Int. J. Non-Linear Mech. 67 (2014) 120–132.
[26] X. Zhang, G. Cheng, H. Zhang, Theoretical prediction and numerical simulation of multi-cell square thin-walled structures, Thin-Walled Struct. 44 (2006) 1185–1191.
[27] T. Tran, S. Hou, X. Han, N. Nguyen, M. Chau, Theoretical prediction and crashworthiness optimization of multi-cell square tubes under oblique impact loading, Int. J. Mech. Sci. 89 (2014) 177–193.
[28] S. Hou, Q. Li, S. Long, X. Yang, W. Li, Design optimization of regular hexagonal thin-walled columns with crashworthiness criteria, Finite Element in Analysis & Design 43 (2007) 555–565.
[29] G. Sun, G. Li, S. Hou, S. Zhou, W. Li, Q. Li, Crashworthiness design for functionally graded foam-filled thin-walled structures, Mater. Sci. Eng.: A 527 (2010) 1911–1919.
[30] M.A. Guler, M.E. Cerit, B. Bayram, B. Gerceker, E. Karakaya, The effect of geometrical parameters on the energy absorption characteristics of thin-walled structures under axial impact loading, Int. J. Crashworthiness 15 (2010) 377–390.
[31] Q. Li, G.P. Steven, O.M. Querin, Y. Xie, Structural topology design with multiple thermal criteria, Eng. Comput. 17 (2000) 715–734.
[32] Q. Li, G.P. Steven, Y. Xie, Thermoelastic topology optimization for problems with varying temperature fields, J. Thermal Stress. 24 (2001) 347–366.
[33] W. Li, Q. Li, G.P. Steven, Y. Xie, An evolutionary shape optimization for elastic contact problems subject to multiple load cases, Comput. Methods Appl. Mech. Eng. 194 (2005) 3394–3415.
[34] Y. Zhang, G. Sun, X. Xu, G. Li, Q. Li, Multiobjective crashworthiness optimization of hollow and conical tubes for multiple load cases, Thin-Walled Struct. 82 (2014) 331–342.
[35] X.G. Song, J.H. Jung, H.J. Son, J.H. Park, K.H. Lee, Y.C. Park, Metamodel-based optimization of a control arm considering strength and durability performance, Comput. Math Appl. 60 (2010) 976–980.
[36] R.J. Yang, N. Wang, C.H. Tho, J.P. Bobineau, Metamodeling development for vehicle frontal impact simulation, J. Mech. Des. 127 (2005) 1014–1020.
[37] S.Q. Shan, G.G. Wang, Metamodeling for high dimensional simulation-based design problems, J. Mech. Des. 132 (2010).
[38] J.G. Fang, Y.K. Gao, G.Y. Sun, Q. Li, Multiobjective reliability-based optimization for design of a vehicledoor, Finite Elem. Anal. Des. 67 (2013) 13–21.
[39] H. Fang, M. Rais-Rohani, Z. Liu, M. Horstemeyer, A comparative study of metamodeling methods for multiobjective crashworthiness optimization, Comput. Struct. 83 (2005) 2121–2136.
[40] Y.K. Gao, F. Sun, Multi-disciplinary optimisation for front auto body based on multiple optimisation methods, Int. J. Vehicle Des. 57 (2011) 178–195.
[41] Y. Zhang, G. Sun, G. Li, Z. Luo, Q. Li, Optimization of foam-filled bitubal structures for crashworthiness criteria, Mater. Des. 38 (2012) 99–109.
[42] J. Sacks, W.J. Welch, T.J. Mitchell, H.P. Wynn, Design and analysis of computer experiments, Statist. Sci. 4 (1989) 409–423.
[43] R. Eberhart, J. Kennedy, A new optimizer using particle swarm theory, in: Micro Machine and Human Science, 1995. MHS'95., Proc. Sixth Int. Symp. IEEE (1995) 39–43.
[44] X. Liao, Q. Li, X. Yang, W. Zhang, W. Li, Multiobjective optimization for crash safety design of vehicles using stepwise regression model, Struct. Multidiscip. Optim. 35 (2008) 561–569.
[45] C.A.C. Coello, G.T. Pulido, M.S. Lechuga, Handling multiple objectives with particle swarm optimization, Evolut. Comput. IEEE Trans. 8 (2004) 256–279.
[46] C.R. Raquel, P.C. Naval Jr, An effective use of crowding distance in multi-objective particle swarm optimization, in: Proceedings of the 2005 conference on Genetic and evolutionary computation, ACM, 2005, pp. 257–264.
[47] G. Sun, G. Li, Z. Gong, G. He, Q. Li, Radial basis functional model for multi-objective sheet metal forming optimization, Eng. Optim. 43 (2011) 1351–1366.
[48] B.S. Yang, Y.S. Yeun, W.S. Ruy, Managing approximation models in multi-objective optimization, Struct. Multidiscip. O 24 (2002) 141–156.
[49] B.S. Jang, D.E. Ko, Y.S. Suh, Y.S. Yang, Adaptive approximation in multi-objective optimization for full stochastic fatigue design problem, Mar. Struct. 22 (2009) 610–632.
[50] G. Sun, X. Song, S. Baek, Q. Li, Robust optimization of foam-filled thin-walled structure based on sequential Kriging metamodel, Struct. Multidiscip. Optim. 49 (2014) 897–913.
[51] J. Fang, Y. Gao, G. Sun, C. Xu, Y. Zhang, Q. Li, Optimization of spot-welded joints combined artificial bee colony algorithm with sequential Kriging optimization, Adv. Mech. Eng. 6 (2014) 573694.
[52] S. Barakat, K. Bani-Hani, M.Q. Taha, Multi-objective reliability-based optimization of prestressed concrete beams, Struct. Saf. 26 (2004) 311–342.

View publication stats